

Structure imaging by atomic force microscopy and transmission electron microscopy of different light emitting species of porous silicon

R. Massami Sasaki, R. A. Douglas, M. U. Kleinke, and O. Teschke

Citation: *Journal of Vacuum Science & Technology B* **14**, 2432 (1996); doi: 10.1116/1.588874

View online: <http://dx.doi.org/10.1116/1.588874>

View Table of Contents: <http://scitation.aip.org/content/avs/journal/jvstb/14/4?ver=pdfcov>

Published by the AVS: Science & Technology of Materials, Interfaces, and Processing

Articles you may be interested in

[Visualization of nanostructured porous silicon by a combination of transmission electron microscopy and atomic force microscopy](#)

Appl. Phys. Lett. **68**, 2129 (1996); 10.1063/1.115607

[Investigation of porous silicon by scanning tunneling microscopy and atomic force microscopy](#)

J. Vac. Sci. Technol. B **12**, 2437 (1994); 10.1116/1.587778

[Electronic structure of lightemitting porous Si](#)


Appl. Phys. Lett. **60**, 1004 (1992); 10.1063/1.106503

[Porous silicon microstructure as studied by transmission electron microscopy](#)

Appl. Phys. Lett. **55**, 1540 (1989); 10.1063/1.102239

[Lattice and atomic structure imaging of semiconductors by high resolution transmission electron microscopy](#)

Appl. Phys. Lett. **47**, 685 (1985); 10.1063/1.96058



A PASSION FOR PERFECTION

PFEIFFER VACUUM

HiPace® M magnetically levitated turbopumps

- Simple installation
- Long service life
- Innovative bearing system

Are you looking for a perfect vacuum solution?
Please contact us!

Structure imaging by atomic force microscopy and transmission electron microscopy of different light emitting species of porous silicon

R. Massami Sasaki

Instituto de Química, Universidade Estadual de Campinas, 13083-970 Campinas, São Paulo, Brazil

R. A. Douglas,^{a)} M. U. Kleinke, and O. Teschke

Instituto de Física Gleb Wataghin, Departamento de Física Aplicada, Universidade Estadual de Campinas, 13083-970 Campinas, São Paulo, Brazil

(Received 6 February 1996; accepted 1 May 1996)

The complex pattern of the nanowire skeletons of different light emitting porous silicon structures is investigated by transmission electron microscopy (TEM) and atomic force microscopy (AFM). Diffraction lines and dark field images are used to identify and determine the crystallite specimen long range order. TEM images give the size and particle orientation, and AFM images show a three-dimensional pattern formed by an interconnecting skeleton of particles. Near infrared photoluminescent porous silicon (0.006 Ω cm) structures show a skeleton of nanosized silicon aggregates which form domains of spatially oriented crystallites. For red photoluminescent samples (4.9 Ω cm) the electron diffraction spots are discontinuously split into tiny intensity maxima. The diameter of the wire structure forming porous silicon as measured by TEM allows us to estimate the distortion of the AFM images due to the finite size of the tip radius. A critical angle $\alpha_0 = 2 \arctan[K/(1-K)]^{1/2}$, where K is the ratio of the height of the structure to the tip diameter was defined and it was shown that for structure walls steeper than α_0 the distortion may be substantial.

© 1996 American Vacuum Society.

I. INTRODUCTION

A debate exists on the precise processes responsible for porous silicon (PS) photoluminescence.¹⁻⁴ A better understanding of the complex structure of skeletons consisting of nanosized particles in different light emitting PS species is required. Increased control over formation morphologies is also of fundamental importance for many applications proposed for these materials. The most adequate techniques to investigate the atomic structure of metal and semiconductor surfaces are provided by scanning tunneling microscopy (STM) and TEM.^{5,6} STM measurements on films thicker than 500 nm revealed instabilities in the tunnel current so that surface topography could not be definitely determined.⁷ In a recent paper, we reported TEM results which reveal the nanostructure of luminescent PS.⁸⁻¹¹ PS surfaces have been previously investigated by using AFM and STM.¹²⁻¹⁴ Theories of image formation have been reported, the most prevalent being the tip sample convolution which is based on purely geometrical considerations assuming a strictly stiff cantilever, with only one degree of freedom in the vertical direction.¹⁵ The essence of the theory is that in each observed image there exists some information about the tip in addition to the information about the sample.

In the experiments described below, we exploit the capabilities of AFM combined with TEM to examine the nature of the structure of PS layers. Moreover, in order to gain a better understanding of the image formation mechanism in AFM, a comparison of AFM and TEM images is also performed. To this end, we report AFM studies of the three-dimensional pattern formed by the PS layer, while TEM

studies give the size and orientation of the nanoparticles.

II. EXPERIMENT

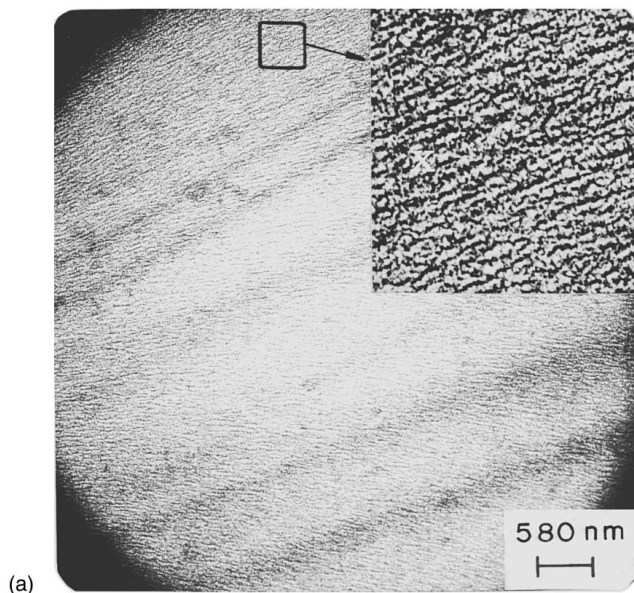
Single-crystal, polished $\langle 100 \rangle$ and $\langle 111 \rangle$ wafers of doped (p - and n -type) silicon of 0.006, 0.4, and 4.9 Ω cm resistivities were cut into rectangles with areas of approximately 1.0 cm². The etching bath was a 50:50 (by volume) solution of 48% HF (Merck) and 95% ethanol (Merck). The samples were etched using a model 273A potentiostat/galvanostat (Princeton Applied Research). After anodization the silicon slab edge was inserted into the TEM for study, as previously described.⁸ TEM examinations were carried out in a Zeiss CEM902 microscope using 80 keV electrons and equipped with an electron energy loss spectrometer (EELS) and an image intensifying camera.

The silicon samples for AFM observations were removed from the electrolyte without removing the liquid adhered to its surface, placed in a glass container, and immersed in liquid nitrogen. The frozen samples were then placed under vacuum (10^{-3} Torr), and their glass containers were immersed in liquid nitrogen. Solution sublimation from the samples took about 2 h. AFM observations were carried out in a TopoMetrix TMX 2000 AFM instrument, using the variable force mode in the repulsive force region. Images were obtained in air on freshly produced surfaces. The room temperature photoluminescence system has been described previously.⁹

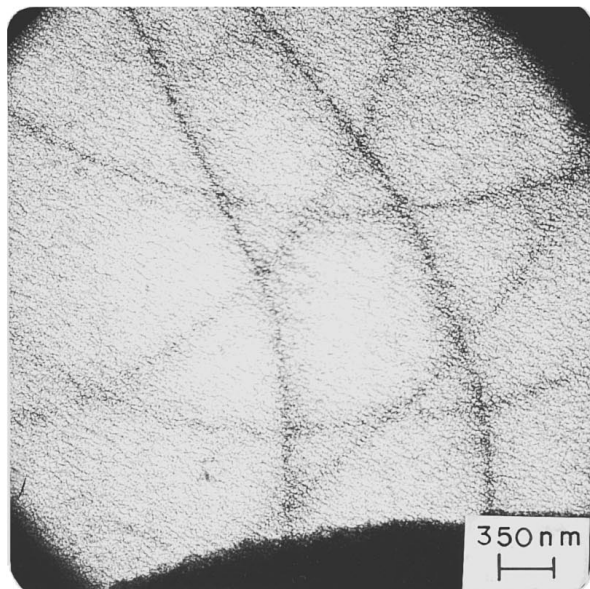
III. RESULTS

Images obtained by TEM from a 0.009 Ω cm, n -type, $\langle 100 \rangle$ oriented silicon sample, anodized at current density of

^{a)}Electronic mail: ross@ifi.unicamp.br



(a)



(b)

FIG. 1. Transmission electron micrographs of the porous silicon structure formed on $\langle 100 \rangle$ oriented silicon, n -type, $0.009 \Omega \text{ cm}$ sample. (a) Inset shows a region with $4\times$ magnification. X indicates a 20-nm-diam particle. Diffraction contrast lines form a pattern of almost straight lines. (b) Curved diffraction contrast lines and microscopic structure.

100 mA/cm^2 , are displayed in Figs. 1(a) and 1(b). This sample shows a near infrared photoluminescence peak at 1.45 eV. Two distinct types of structures can be seen in Fig. 1(a): a pattern of columnar dark spots $\sim 4 \text{ nm}$ in diameter over the entire PS surface and an array of holes (whitish areas) $\sim 25 \text{ nm}$ across, forming a structure of pores perpendicular to the plane of the silicon slab and exhibiting wall dimensions of the order of $\sim 30 \text{ nm}$. In addition, Fig. 1(a) shows diffraction contrast lines on the surface of the PS films. These contrast lines arise from the etching action when the crystallites forming the crystal are slightly tilted. It is also

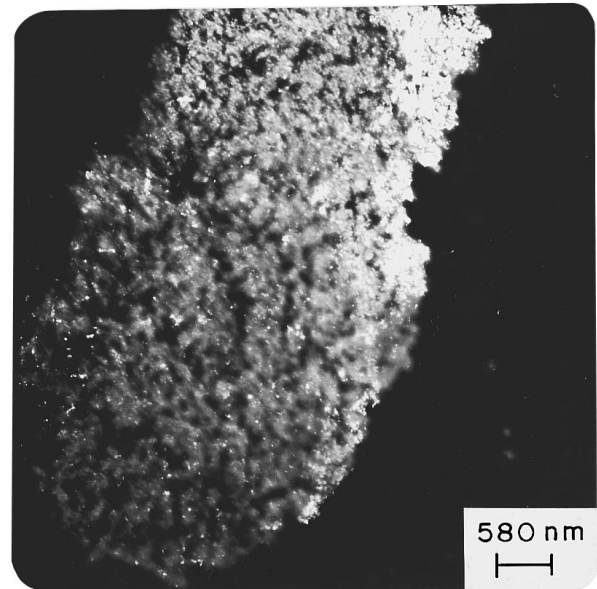
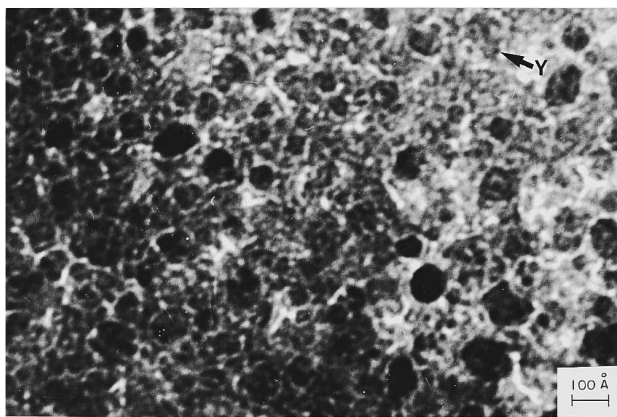


FIG. 2. Dark field images obtained by TEM in the $\{311\}$ directions of a porous silicon structure formed in $\langle 100 \rangle$ oriented silicon n -type, $0.009 \Omega \text{ cm}$. The long-range ordering resulting from the original crystalline structure is given by the width of the brightest region ($\sim 500 \text{ nm}$).

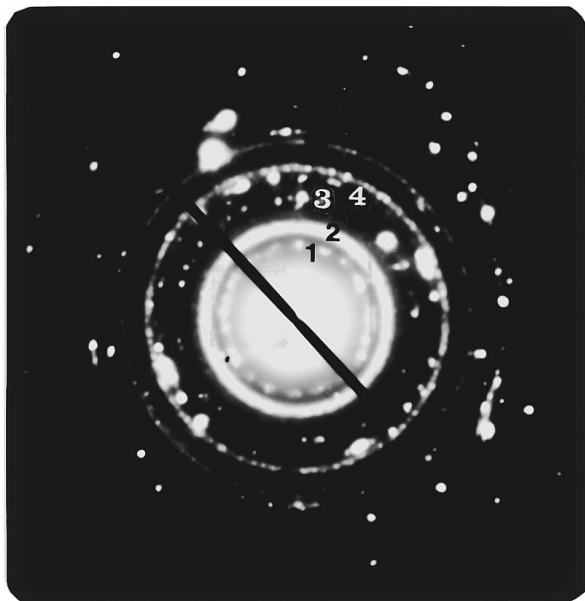
evident that when the misorientation of the crystallites distorts the original grid into curved lines, the dark fringes are curved, as shown in Fig. 1(b).

In order to check the crystallites spatially variable orientation in the etched samples, dark field images, as shown in Fig. 2, were obtained by TEM. Spots corresponding to the $\{111\}$, $\{220\}$, $\{311\}$, $\{400\}$, $\{331\}$, and $\{422\}$ diffraction were observed. The dark field image for the $\{311\}$ direction (Fig. 2) clearly shows that the nanocrystals in the brightest area of the photograph are preferentially aligned along this orientation. The long-range ordering resulting from the original crystalline structure in the sample is of the order of $\sim 500 \text{ nm}$.

Figure 3(a) shows the TEM image of a $4.9 \Omega \text{ cm}$, p -type, $\langle 100 \rangle$ oriented silicon sample, anodized at a current density of 5 mA/cm^2 . This sample shows a photoluminescence peak at 1.8 eV. The shape of the etched parts of the sample are emphasized by a whitish color. The structure of the anodized silicon is seen to be composed of highly isolated columns [marked Y in Fig. 3(a)] as small as 15 \AA cross-section diameter. Figure 3(b) shows that the asterism of the electron diffraction spots is discontinuously split into tiny intensity maxima. Spots corresponding to the $\{311\}$, $\{331\}$, and $\{533\}$ diffraction were observed [indicated by 1, 3, and 4 in Fig. 3(b)]. This observation indicates that segmented crystallites are produced, which are relatively undistorted among themselves although differing slightly in orientation from their neighbors. The etched lattice is formed by an aggregate of comparatively strain-free subgrains separated from one another and having nearly the same orientation as the original crystal.



(a)



(b)

FIG. 3. (a) TEM images of porous silicon structure formed by anodizing a 4.9 Ω cm $\langle 100 \rangle$ oriented, *p*-type silicon samples. Y indicates a particle with a diameter of ~ 15 Å. (b) Electron anodized diffraction pattern of porous silicon obtained by TEM showing spots corresponding to the $\langle 311 \rangle$, $\langle 331 \rangle$, and $\langle 533 \rangle$ diffraction, indicated by 1, 3, and 4.

The surface topography of PS samples was then investigated by AFM. An image corresponding to a central position in the 1 cm diameter, 0.009 Ω cm samples, anodized with a current of 100 mA/cm² during 20 min, is shown in Fig. 4. Etched holes are emphasized by dark color. A skeleton structure is observed, which is formed by a pattern of large holes having diameters of ~ 1 μ m (dark regions, indicated by Y). The walls of these pores have dimensions of this order as well.

Silicon tips from Park Instruments [UltraleverTM(Si) and MicroleverTM (SiN)] were used to obtain improved spatial resolution. An image obtained by AFM (MicroleverTM tip) from a *p*-type 4.9 Ω cm $\langle 100 \rangle$ oriented silicon sample, anodized during 30 min at 5 mA/cm² current density, is displayed in Fig. 5. These samples show a red photoluminescent peak

at 1.8 eV.¹⁰ The image shows a pattern of columns (light isolated spots) over the entire PS surface. A more detailed mapping of the PS formed structure is shown by its profile. Typical profiles of this sample observed by AFM show valleys and hills as small as 55 Å wide [see Fig. 6(a) obtained with the MicroleverTM tip and Fig. 6(b) with the UltraleverTM tip].

IV. DISCUSSION

A. TEM observations, diffraction lines, and dark field images

The results above demonstrate that PS layers formed during silicon anodization of different light emitting species also have different structures (see Figs. 1–3). Diffraction lines and dark field images are used to identify and define the crystallite specimen long-range order. The long-range order shown in Fig. 2 is ~ 500 nm. Figure 3(b) shows that PS formed on 4.9 Ω cm samples is composed of small loosely connected crystallites, as previously reported¹⁶ PS layers are therefore formed by slightly disoriented lattice segments or subgrains, separated by etched holes. TEM images give the sizes and particle orientations (Figs. 1–3).

B. Observation by AFM and TEM

A comparison of TEM and AFM images of samples was then performed. Figures 1(a) and 1(b) are TEM images and Fig. 4 depicts an AFM image of the 0.009 Ω cm, *n*-type, $\langle 100 \rangle$ oriented silicon substrate each showing different aspects of the porous nanosized structure. The AFM images give a three-dimensional view of the skeleton structure of PS which cannot be observed by TEM. This three-dimensionality allows the visualization of the interconnecting structure.

An AFM image corresponding to a red-photoluminescence sample is presented in Figs. 5 and 6. Note that it was not possible to resolve features smaller than those shown in this figure. The discrepancy between the PS surface shown by TEM and the one shown by AFM is due to the response of the probe tip to the force exerted by the surface structure. AFM images are a reconstruction from digital data obtained from a probe tip response to a sample's topography as the tip is scanned across the surface. Studies involving structures highly three-dimensional, as PS layers, can be complicated by the fact that although the vertical resolution is usually excellent, the AFM produces distorted lateral features on the steeply inclined sides of nanoparticles. The effect of the finite curvature of the tip in AFM imaging has been noted by several authors.^{17–21} Therefore a knowledge of the tip geometry is of fundamental importance.

C. AFM image distortions and geometrical resolution limitations

The distortion of an AFM image is illustrated by the response of a conical tip with an apex tip radius R_T to various structures as shown in Figs. 7(a) and 7(b). Two situations can be distinguished, namely $\alpha < \alpha_0$ or $\alpha \geq \alpha_0$, where

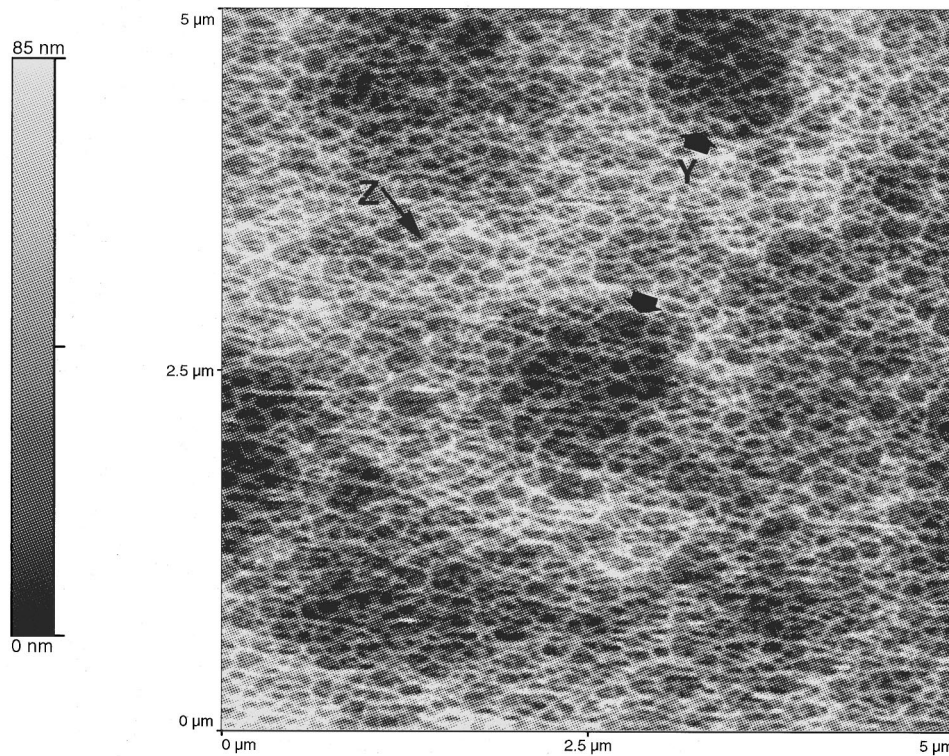


FIG. 4. An AFM image of a porous silicon etched in $\langle 100 \rangle$ oriented silicon, n -type, $0.009 \Omega \text{ cm}$. It shows a skeleton structure of holes and walls formed by a substructure of ~ 40 -nm-thick walls, indicated by Z.

$\alpha_0 = 2 \arctan[K/(1-K)]^{1/2}$, $K = h/2R_T$, h is the height of the object, R_T is the apex radius, and α is angle of rise or fall of the structure. Figure 7(b) shows that for $\alpha < \alpha_0$, the increase in the width of a structure in the sample is given by $R_T \sin(\alpha/2)$ for each rise or fall of the sample structure. This value does not depend on the height h of the structure.

For $\alpha \geq \alpha_0$ and small values of h ($h/R_T < 0.3$) only the spherical apex surveys the structure. Figure 7(a) shows the observed profiles for this situation, while Fig. 8(a) displays

the unobserved region d or “hole region” and Fig. 8(b) the critical angle α_0 as a function of the object height (h) for the tip apex radii of 200, 50, 30 and 15 Å. The distortions introduced do not affect the height, but only the width and the increase in the width will depend on the height (h) and angles (α 's) of the structure. Table I gives the values of the calculated full width at half height for objects of various heights h and apex tip radii R_T . The object is a symmetrical trapezoid with a flat horizontal top of 15 Å width, and α is

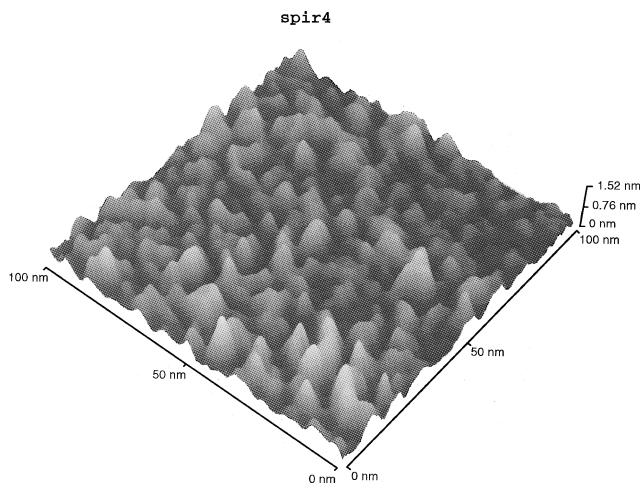


FIG. 5. An AFM image of p -type, $4.9 \Omega \text{ cm}$ $\langle 100 \rangle$ oriented silicon sample anodized during 30 min at 5 mA/cm^2 current density. It shows a pattern of columns over the entire surface.

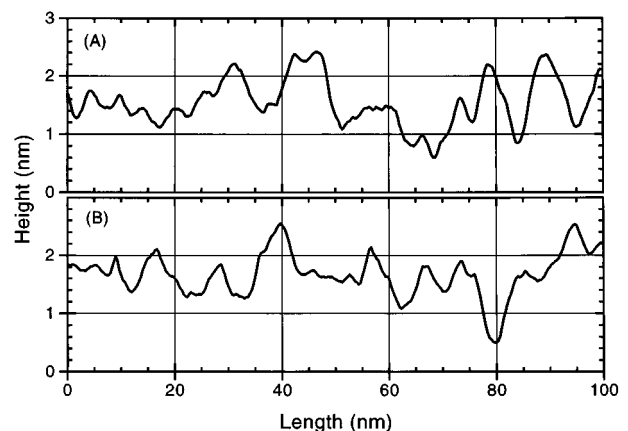


FIG. 6. Typical profiles of the sample of Fig. 5 with (a) a Microlever™ Si tip; (b) an Ultralever™ Si tip.

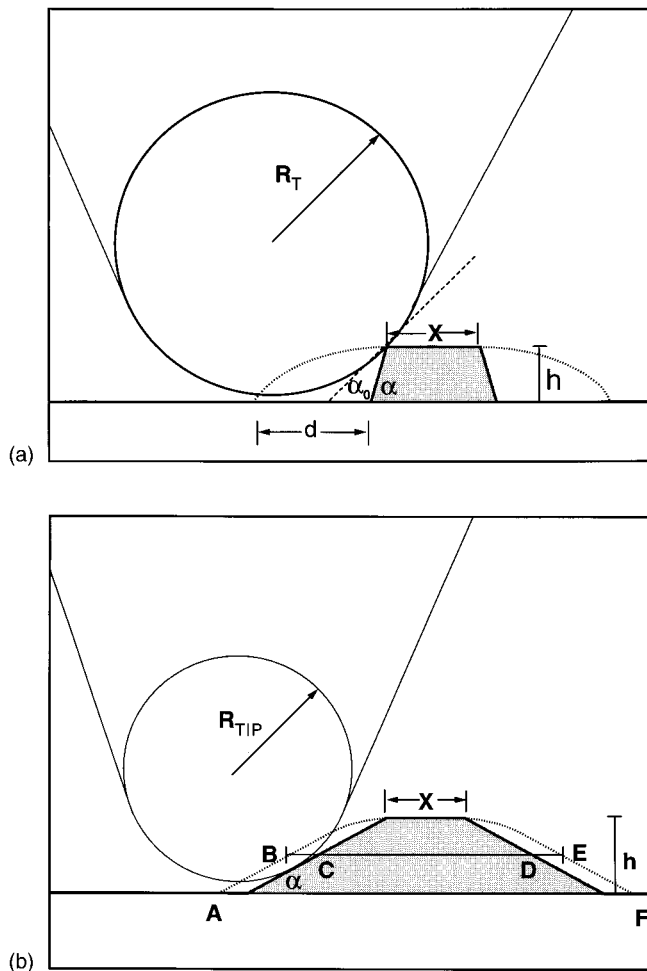


FIG. 7. Distortion of an AFM image illustrated by the response of a tip of radius R_T to a step structure which rises at an angle α to a vertical height h . (a) α larger than the critical angle α_0 ; (b) α smaller than the critical angle α_0 .

the angle of rise (or fall) of the structure. Observe that the measured particle width depends critically on both the particle height and the tip radius.

D. Porous silicon AFM formed images

The spatial resolution of the TEM images is 15 \AA , while that of the AFM depends critically on the profile of the probe tip and sample. When the tip apex radius is of a magnitude similar to the one of the sample structure, the distances between adjacent peaks in the samples are well reproduced in the observed image. Also, there is less distortion of peaks than of valleys. The depth of valleys in the image is strongly dependent on the radius of the tip. The radii of tips were determined from the profiles shown in Fig. 6. For the MicroleverTM tips the estimated radius obtained from the profiles shown in Fig. 6(a) is $48 \pm 10 \text{ \AA}$ and for the UltraleverTM tips [Fig. 6(b)] the radius is equal to $30 \pm 6 \text{ \AA}$.

The porous silicon layers are formed by a skeleton structure of $\sim 15 \text{ \AA}$ diameter cylinders as shown in Fig. 3(a). The profiles present peaks with heights around 10 \AA . Using this height value and the estimated radius of the tips, the critical

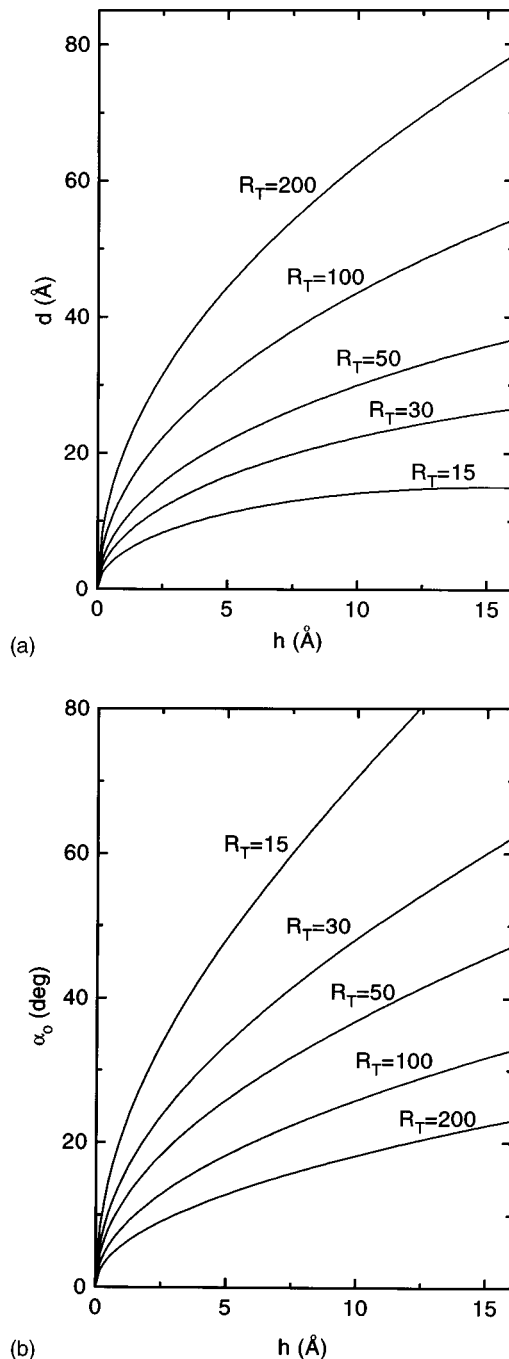


FIG. 8. (a) Value of the unobserved region length d as a function of the vertical height for various tip radii R_T . (b) Critical angle value α_0 as a function of the vertical height for various tip radii R_T .

angle for the UltraleverTM and MicroleverTM tips are equal to 60° and 42° , respectively, which are larger than the observed α 's of 10° to 15° , as illustrated in Fig. 7(b). Thus the true width is the measured width minus $R \sin(\alpha/2)$ for both the rise and the fall. Isolated peak profiles shown in Figs. 6(a) and 6(b) were measured and the ascending and the descending angles calculated as well as the radii of the peaks. The smallest particle width was estimated to be $15 \pm 4 \text{ \AA}$ (for the MicroleverTM tip) and $15 \pm 8 \text{ \AA}$ (for the UltraleverTM tip).

TABLE I. The observed full widths at half-maximum (FWHM) of structures with $\alpha > \alpha_0$, where the width is 15 Å at the top for various heights from 2 to 15 Å and for tips with apex radii of 200, 100, 50, 30, and 15 Å. No specification is made of the half angle of the cone, so that no values of FWHM are given for $h > 0.3R_T$ where this parameter would be necessary.

h (Å) \ R (Å)	200	100	50	30	15
15	124	91	68
10	104	77	59	48	...
05	78	59	46	39	32
02	55	43	35	30	26

V. CONCLUSIONS

In conclusion, this work has shown that different structures are responsible for near infrared and red luminescent PS. Diffraction lines and dark field images are used to identify and define the crystallite specimen long-range order. TEM images give the size and particle orientation, and AFM images show a three-dimensional pattern formed by an interconnecting skeleton of particles. The spatial resolution of the TEM images is 15 Å, while that of the AFM depends critically on the profile of the probe tip and the height and slope of the observed structure.

The measured diameter wire structure forming porous silicon structure by AFM and TEM allows us to calculate the distortion of the AFM images due to the finite size of the tip radius. A critical angle $\alpha_0 = 2 \arctan[K/(1-K)]^{1/2}$, where K is the ratio of the height of the structure to the tip diameter, was defined and substantial distortions were observed for structure walls that are steeper than the critical angle.

ACKNOWLEDGMENTS

The authors are grateful to L. O. Bonugli and J. R. Castro for technical assistance and FAPESP 93/0961-5, CNPq 520060/93-8, and FAEP/UNICAMP 0726/94 for financial support.

- ¹L. T. Canham, *Appl. Phys. Lett.* **57**, 1046 (1990).
- ²F. Buda, J. Kohanoff, and M. Parrinello, *Phys. Rev. Lett.* **69**, 1272 (1992).
- ³J. P. Proot, C. Delerue, and G. Alan, *Appl. Phys. Lett.* **61**, 1948 (1992).
- ⁴S. Furukawa and T. Miyasato, *Jpn. J. Appl. Phys.* **27**, L-2207 (1988).
- ⁵D. Sarid, *Scanning Force Microscopy* (Oxford University, Oxford, 1991), and references cited therein.
- ⁶G. Binnig, H. Rohrer, C. Gerber, and E. Weibel, *Appl. Phys. Lett.* **40**, 178 (1982).
- ⁷M. Enachescu, E. Hartmann, A. Kux, and F. Koch, *J. Lumin.* **57**, 191 (1993).
- ⁸O. Teschke, M. C. Gonçalves, and F. Galembeck, *Appl. Phys. Lett.* **63**, 1348 (1993).
- ⁹O. Teschke, F. Alvarez, L. R. Tessler, and M. U. Kleinke, *Appl. Phys. Lett.* **63**, 1927 (1993).
- ¹⁰O. Teschke, *Appl. Phys. Lett.* **64**, 1986 (1994).
- ¹¹O. Teschke, F. Galembeck, M. C. Gonçalves, and C. V. Davanzo, *Appl. Phys. Lett.* **64**, 3590 (1994).
- ¹²J. M. Gomez-Rodriguez, A. M. Baro, and V. P. Parkhutik, *Appl. Surf. Sci.* **44**, 185 (1990).
- ¹³G. B. Amisola, R. Behrensmeier, J. M. Galligan, F. A. Otter, F. Namavar, and N. M. Kalkoran, *Appl. Phys. Lett.* **61**, 2595 (1992).
- ¹⁴V. P. Parkhutik, J. M. Abella, J. M. Martinez-Duart, J. M. Gomez-Rodriguez, A. M. Baro, and V. I. Shershulsky, *Appl. Phys. Lett.* **62**, 366 (1993).
- ¹⁵C. Odin, J. P. Aimé, Z. El Kaakour, and T. Bouhacina, *Surf. Sci.* **317**, 321 (1994).
- ¹⁶K. Barla, R. Herino, G. Bomchil, J. C. Pfister, and A. Freund, *J. Cryst. Growth* **68**, 727 (1984).
- ¹⁷Ph. Niedermann and O. Fisher, *J. Microsc.* **152**, 93 (1988).
- ¹⁸M. Stedman, *J. Microsc.* **152**, 611 (1988).
- ¹⁹G. Reiss, J. Vancea, H. Wittman, J. Zweek, and H. Hoffmann, *J. Appl. Phys.* **67**, 1156 (1990).
- ²⁰K. L. Westra, A. W. Mitchell, and D. J. Thomson, *J. Appl. Phys.* **74**, 3608 (1993).
- ²¹J. E. Griffith and D. A. Grigg, *J. Appl. Phys.* **74**, R 83 (1993).